Journal of Materials Chemistry A

ROYAL SOCIETY OF CHEMISTRY

PAPER

View Article Online
View Journal

Cite this: DOI: 10.1039/d5ta05129k

Subsurface hydrogen, curvature, and strain: lessons from electro-reduction of benzaldehyde on nano-structured Pd catalysts

Sri Krishna Murthy Padavala,[af] Sumudu Nimasha,[b] K. A. U. Madhushani,[c] Long Luo,[bc] Dongsheng Li,[d] Hyoju Park,[d] Hua Zhou,[e] Nanjun Chen,[d] Qin Pang,[d] Peter V. Sushko *[d] and Kelsey A. Stoerzinger *[a]

The unique ability of palladium (Pd) to absorb hydrogen and form a bulk hydride is vital for chemical transformations that involve hydrogenation reactions. Nano-structured Pd catalysts offer a promise of tuning these reaction rates by exploiting variations of reactant binding energies depending on the surface structure and morphological constraints that result in inhomogeneous strain. However, the interplay between the nano-structure of Pd and the ability of Pd to adsorb (and absorb) hydrogen as well as other reactive species needs to be better understood for a rational understanding of competitive chemical transformations at Pd surfaces. We consider the effects of the surface corrugation, strain, and subsurface Pd hydride on the reduction of benzaldehyde to benzyl alcohol in two qualitatively different samples – Pd nanoparticles and Pd gels formed by quasi-one-dimensional chains of these nanoparticles. Our electrochemical measurements and computational modelling suggest that surface concave sites, inherent to Pd gels, facilitate hydrogen transfer to the Pd subsurface region, thus weakening benzaldehyde binding to the surface. This effect is further modulated by the strain, depending on the local coordination environment on the corrugated surface. These findings demonstrate how structurally complex samples in the form of gels provide degrees of freedom for controlling the behavior of metal catalysts that are not available in isolated nanoparticles, which paves the way for new approaches in the design of catalytic materials and synthesis of metal hydrides.

Received 24th June 2025
Accepted 19th August 2025

DOI: 10.1039/d5ta05129k

rsc.li/materials-a

1 Introduction

Hydrogenation reactions underpin numerous chemical conversions and energy storage reactions, often driven by platinum group elements like palladium.[1] Palladium is unique, however, in its ability to transform into a metal hydride at low equivalent hydrogen pressures—making its active state intricately linked to the processing conditions.[2] The formation of the hydride phase depends on a balance of kinetic rates at the surface and within the bulk;[3–5] deterministic control requires precise synthesis science to obtain surface microenvironments favoring hydride formation on and into the lattice[6,7] at rates greater than hydride consumption *via* surface-mediated processes. The presence of hydrogen in the subsurface decreases the Pd work function[8] and leads to a local charge density redistribution, as well as an increase in the lattice constant.[9,10] As such, the hydride phase may favor some reactions and disfavor others.[11,12] Accordingly, our ability to tailor catalytic functions will be enhanced with the ability to predictively promote or suppress the formation of the hydride phase.

The *in situ* formation of the hydride phase can be limited by the co-adsorption of strongly bound organic reactants, where amongst a range of carbonyl functionalities, benzaldehyde (BZ) binds the strongest.[13] BZ is a model bio-oil compound containing one aromatic ring and a formyl substituent whose hydrogenation is often used as a proxy for the conversion of biomass to biofuels.[14] This process can be driven either by the temperature and pressure of hydrogen—termed thermocatalytic hydrogenation (TCH)—or by applying electrical bias—termed electrocatalytic hydrogenation (ECH).[13,15–20] At the applied electrochemical potentials such that protons and electrons can together reduce BZ (with two H^+ and two e^- required to produce benzyl alcohol, BnOH), the surface-mediated recombination of H^+/e^- pairs resulting in H_2 gas, *i.e.*, the hydrogen evolution reaction (HER) is also a possible outcome. Since these electrochemical potentials are also ones where

[a]Department of Chemical Engineering and Materials Science, University of Minnesota, Twin Cities, Minnesota 55455, USA. E-mail: zinger@umn.edu
[b]Department of Chemistry, Wayne State University, Detroit, Michigan 48201, USA
[c]Department of Chemistry, University of Utah, Salt Lake City, Utah 84112, USA
[d]Physical and Computational Sciences Directorate, Pacific Northwest National Laboratory, Richland, Washington 99354, USA. E-mail: peter.sushko@pnnl.gov
[e]Advanced Photon Source, Argonne National Laboratory, Lemont, Illinois 60439, USA
[f]Lam Research Corporation, Building B, 11155 SW Leveton Drive, Tualatin, OR 97062, USA

palladium hydride (PdH_x) formation is thermodynamically favorable,[18,19,21–23] a strong coupling between these processes can be expected. More broadly, because PdH_x formation requires a high surface coverage of adsorbed hydrogen and its facile diffusion into the lattice, hydride formation can be influenced by the extent of adsorption of bulky organic molecules on the surface. The adsorption energies of these organic species would be anticipated to vary strongly with local coordination and confinement. In contrast, the binding energy of the adsorbed H is likely less dependent on this local coordination, while its diffusion through the lattice is highly related to surface strain and void volume.

Here, we investigate how the mutual interplay between Pd morphology and surface structure, BZ and H competitive adsorption, and strain influence the concomitant hydride formation and BZ hydrogenation. We approach these questions by controlling the starting catalyst state and tailoring catalyst morphology to manipulate the drivers of hydride formation. Specifically, in contrast to previous studies of ECH, which started from a PdH_x state,[13,15–20,24,25] we rigorously strip intercalated H to separate the effects of Pd and PdH_x on the kinetics of ECH. This approach is used to reveal the effects of sample morphology by comparing the kinetics of hydrogenation processes in Pd NPs and in networks of interconnected Pd NPs (denoted as Pd gels). We show, through experiments and simulations, that Pd gels weaken BZ binding relative to H, enabling PdH_x formation at much higher BZ concentrations (C_{BZ}) than in Pd NPs. This effect is attributed primarily to two factors: (i) the grain boundaries (GBs) present in Pd gels give rise to concave surface regions where weaker BZ binding and negative curvature allow for H adsorption, and (ii) subsequent H absorption into the subsurface layer induces charge density redistribution that further lowers BZ binding. GBs may also promote PdH_x formation through facile H-diffusion. These studies shed light on the complex interplay between surface chemical processes, as represented by ECH and HER, and the Pd to PdH_x transformation accompanying these processes, providing guiding principles for materials synthesis to target desired catalyst reactivity.

2. Methods

2.1. Synthesis of Pd nanoparticles and GB-rich nanoparticle assemblies

Pd NPs were synthesized as follows. First, 10.0 mL of 70.0 mM sodium citrate aqueous solution and 20.0 mL of 7.0 mM K_2PdCl_4 aqueous solution were added to 400.0 mL deionized water under constant stirring at room temperature. Then, 5.0 mL of 60.0 mM $NaBH_4$ aqueous solution was added to the mixture after one minute. Upon adding $NaBH_4$, the solution immediately turned brown, indicating the formation of Pd NPs. The solution was stirred for another 30 min to achieve homogeneous NP distribution. The GB-rich Pd NP assembly was prepared using a method reported in detail elsewhere.[26] First, the concentration of the Pd NPs in the solution was increased by a factor of 10 using rotary evaporation. Then, the preconcentrated Pd NP solution was subjected to electrochemical processing to form the assemblies using a three-electrode setup with two ~1 cm × 2 cm Pt foils as the working and counter electrodes and an Ag/AgCl/saturated KCl reference electrode. Before use, the Pt foils were electrochemically cleaned in 0.5 M H_2SO_4 by cycling the electrode potential between −0.1 and 1.1 V *vs.* RHE at a scan rate of 100 mV s^{-1} until their voltammogram stabilized. An electrode potential of −2.0 V *vs.* Ag/AgCl was applied to the concentrated Pd NP solution to promote the assembly of Pd NPs. During this process, the NP solution turned colorless over several hours. The NP assembly (gel sample) appeared either precipitated at the vial bottom or attached to the surface of the working electrode. The synthesized NP gel was washed by adding and removing deionized water 10 times over the course of a week. After cleaning, X-ray photoelectron spectra were taken to characterize the surface content. The C 1s peak (288 eV) of the C=O surface functional group of sodium citrate ligands had disappeared, indicating that sodium citrate ligands were effectively removed from the Pd NPs during the assembly and washing steps.

2.2. Electron microscopy

High-angle annular dark-field scanning transmission electron microscopy (HAADF-STEM) images were obtained using a Thermo Fisher Scientific Themis Z (probe Cs-corrected TEM, 300 kV).

2.3. X-ray Diffraction (XRD)

High-resolution XRD measurements were carried out at 12-ID-D beamline at the Advanced Photon Source of Argonne National Laboratory. The X-ray energy was 20 keV (wavelength: 0.61992 Å). X-ray measurement geometry was calibrated using a standard CeO_2 reference powder to make the proper conversion between X-ray detector images to XRD pattern as a function of scattering angle 2θ.

2.4. Computational modeling

The interactions between Pd, H, and BZ and the effect of strain on these interactions were investigated using *ab initio* simulations within the periodic slab models representing the Pd(111) surface (Fig. 1) and the GB-rich Pd gel sample (Fig. 3 and S6). The latter was modeled using a supercell containing two Σ3 (111) twin boundaries and a corrugated surface terminated with (111) planes. This model was used to examine the energetics of the H adsorption and absorption as well as BZ binding to Pd and PdH_x in the presence of uniaxial (tensile or compressive) strain. Supercell lattice parameters, the corresponding k-meshes for Brillouin zone integration, and strain conditions are discussed in the main text for each slab model. The calculations were performed within the density functional theory (DFT) formalism as implemented in the VASP code.[27,28] The Perdew–Burke–Ernzerhof (PBE) exchange-correlation functional[29] and projected augmented wave potentials were used throughout.[30] The plane wave basis set cutoff was 500 eV; the total energy convergence criterion was set to 10^{-5} eV. The DFT-D3 method of Grimme with zero-damping function was used to apply the van der Waals correction for the BZ binding energies

in specific cases.[31] The H atom interaction energies were calculated relative to the energy of the gas-phase H_2 molecule. The charge density distribution was analyzed using the Bader approach.[32,33]

2.5. Pd Gel and NP ink preparation for electrochemical measurements

To make the Pd gel ink for electrode fabrication, 500 μL of ~2 mg mL^{-1} sonicated aqueous suspension was mixed with 250 μL Millipure water and 250 μL isopropyl alcohol (IPA) and subsequently sonicated for 15 min. 100 μL of 0.05 wt% Nafion 117 solution (diluted from 5 wt% Nafion 117 solution, Sigma-Aldrich, using 70 : 30 IPA: Millipure water) was then added, followed by sonication for 5 min. Two Pd NP inks were considered: one with ligated NPs used as gel precursors (where the ligand is stripped electrochemically) and one of commercial 20 wt% Pd/C (Premetek). The Pd NP ink was prepared using a procedure from the literature.[18] Briefly, 2 mL of IPA was added to 4 mg of 20 wt% Pd/C NPs and sonicated for 15 min. Then, 10 μL of 5 wt% Nafion 117 solution was added and sonicated for 15 min.

2.6. Adsorption isotherms

The BZ adsorption isotherm experiment was carried out using the rotating disk electrode setup with the working electrode (WE) rotated at 400 rpm during the isotherm. A GC disk with Pd catalyst ink was the WE, Ag/AgCl (4 M KCl filling solution, Pine Research Instrumentation, Inc.) was used as a reference electrode, and a Pt wire was used as the counter electrode. 100 mL of 3 M acetate buffer (Sigma-Aldrich, pH 5.2) was used as the electrolyte. The electrolyte was initially bubbled with N_2 for an hour and then continuously throughout the experiment to deaerate it. The reported voltages are *iR* corrected with *R* measured using electrochemical impedance spectroscopy at the open-circuit potential.

2.7. Conversion experiments

The conversion experiments were carried out in a glass H-cell. 25 mL of 3 M pH 5.2 acetate buffer (Sigma-Aldrich) was used in both compartments with a Nafion 117 membrane (FuelCell-Store) separating them. Prior to use, the Nafion 117 membrane was soaked in Millipure water. The WE was a carbon felt (3.18 mm thick, 99%, Alfa Aesar) attached to a graphite rod (Becker Brothers), onto which 102 μL of the Pd inks were dropcasted and dried on a hot plate maintained at 50 °C for 2 h. An Ag/AgCl reference electrode (CH Instruments, Inc.) was placed in the catholyte alongside the WE and a graphite rod (counter electrode) was placed in the anolyte. A Biologic VSP-300 potentiostat was used to control the potential applied to the WE. The catholyte was bubbled with nitrogen (N_2) for 20 minutes to deaerate the electrolyte. Next, a CV at 50 mV s^{-1} was performed from 0.05 V *vs.* RHE to 1.2 V *vs.* RHE to quantify the oxide stripping area to obtain the exposed surface area, as shown in Fig. S1.[34] The electrode was conditioned by performing a CV scan from 0 V *vs.* RHE to −0.3 V *vs.* RHE at 50 mV s^{-1} for 3 cycles. For select cases, any residual hydride was then stripped by holding at 0.45 V *vs.* RHE until the current decayed to less than 0.2 μA cm_{ECSA}^{-2} to obtain Pd in the metallic phase. Then, BZ was added to get the required BZ concentration in the electrolyte. 85% ohmic compensation was done during the conversion experiment based on the expected current from initial CVs, with *R* obtained by impedance at open circuit voltage, and the remaining 15% correction was done after the experiment. 0.2 mL samples were taken at specified intervals from the catholyte compartment, with the samples being collected in 30–40 s, as letting the WE go to open circuit potential can give some H-stripping. The catholyte samples were analyzed using an Agilent Technologies reverse phase-high performance liquid chromatograph (RP-HPLC) equipped with a C18 column and a UV-Vis detector. The RP-HPLC solvents were water and acetonitrile (ACN), both buffered with 1% formic acid. A sample injection of 2 μL with a 10–60% ACN gradient over a 10 minutes period (total run time of 20 minutes)

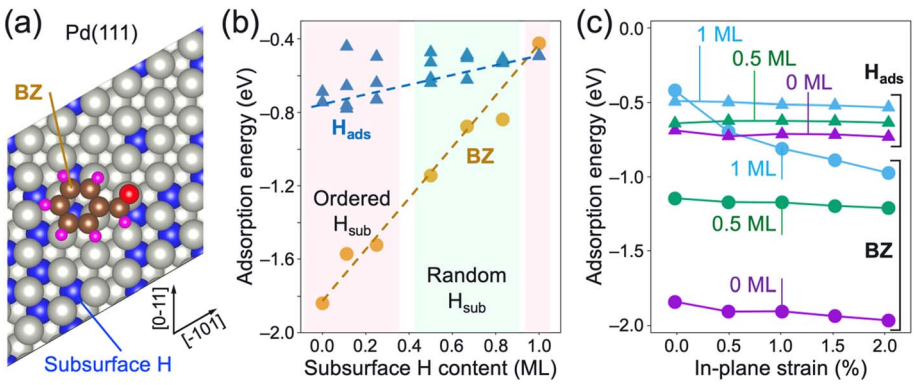

Fig. 1 The stability of BZ adsorbed on the Pd(111) surface is modulated by the amount of subsurface H (H_{sub}) and lattice strain. (a) The Pd(111) terrace was represented by a periodic slab of 6 × 6 lateral supercell, four atomic planes thick, with ordered (2 × 2 and 3 × 3) and random arrangements of H_{sub} (blue) at the octahedral interstitial sites located immediately under the outermost Pd plane. (b) The magnitudes of the BZ and H adsorption energies decrease linearly with increasing H_{sub} concentration. (c) Lateral tensile strain strengthens the BZ binding to the surface (circles) in the case of high H_{sub} concentrations (shown in (c) in ML) and has a negligible effect on the H_{ads} binding.

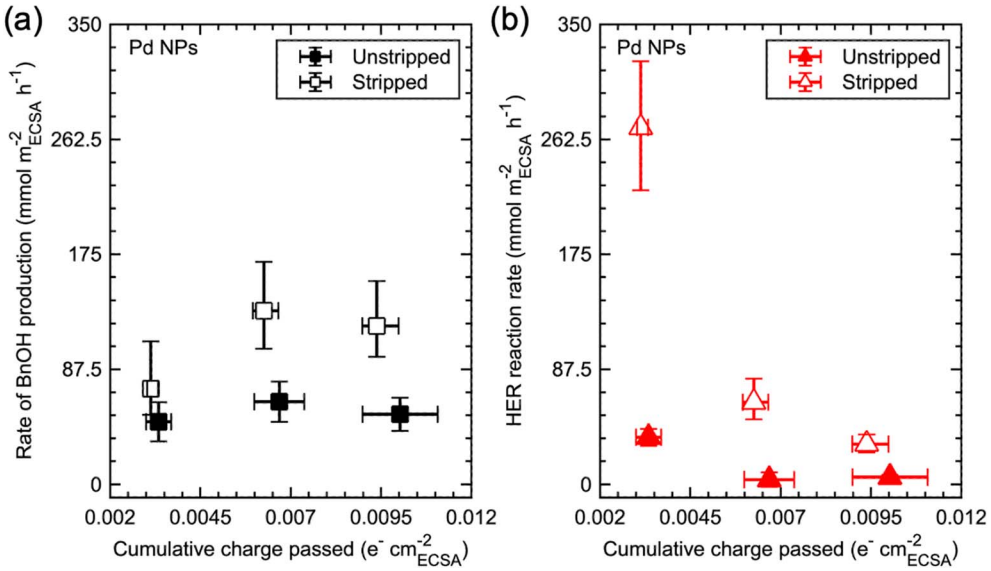

Fig. 2 Reaction rates for stripped and unstripped Pd NPs for 20 mM BZ at −0.1 V *vs.* RHE for (a) electrocatalytic hydrogenation (ECH) and (b) hydrogen evolution reaction (HER) as a function of the cumulative charge passed per Pd surface area. Error bars denote the maximum deviation from the average across three measurements. In both cases, the reaction rates are higher for the stripped (metallic) Pd NPs.

was used. Detection was made at 210 nm and 254 nm wavelength light for BnOH and BZ,[35] respectively, in the samples.

3. Results and discussion

3.1 The effect of subsurface hydrogen and strain on BZ adsorption

To illustrate the coupling between co-adsorbed BZ and H and the role of the Pd surface in modulating their interactions, we evaluate the effects of the lattice strain and H content on the BZ adsorption energies for the case of Pd(111), represented using a periodic slab with the 6 × 6 (16.5 × 16.5 Å^2) lateral supercell and the thickness of four atomic planes (Fig. 1a). The out-of-plane supercell parameter was fixed at 30 Å, leaving the vacuum gap of over 23 Å. The Pd hydride phase was simulated by incorporating H at the interstitial sites near the surface only to capture the qualitative effect of the adsorbed and absorbed species on the binding energies in this system. Therefore, we

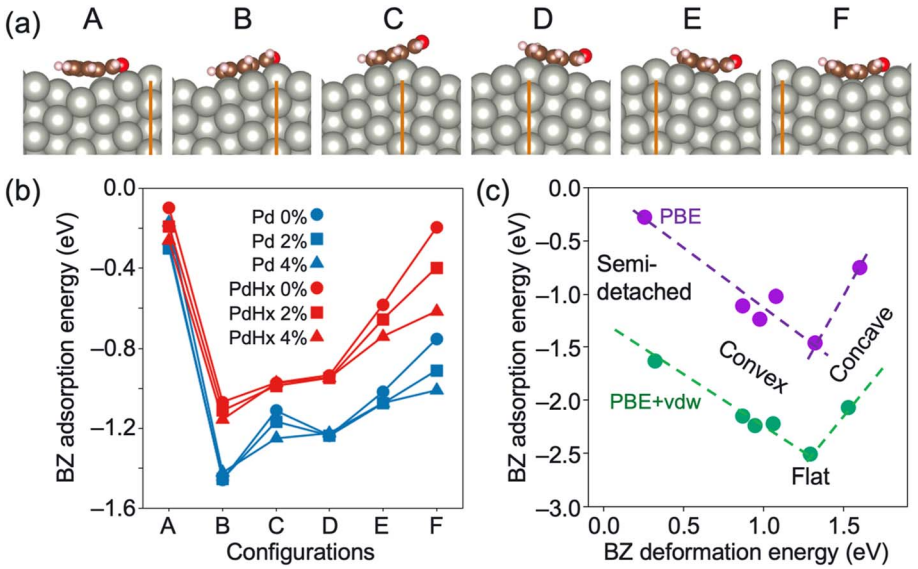

Fig. 3 (a) Configurations of the BZ molecule adsorbed on the corrugated Pd surface (see Fig. S6). The vertical orange line indicates the location of one of the Σ3(111) GBs; it is shown to guide the eye. (b) BZ adsorption energies on the surfaces of pure Pd (blue) and PdH_x (red), where hydrogen occupies octahedral interstitial sites under the top Pd plane only. Binding energies corresponding to the 0, 2, and 4% tensile strain are shown with circles, squares, and triangles, respectively. (c) Trends of the BZ E_{ads} *vs.* deformation energy of the molecule, calculated with (green) and without (purple) van der Waals (vdW) correction, indicate weaker BZ binding at the corrugated Pd surfaces (see also Fig. S7 and S8).

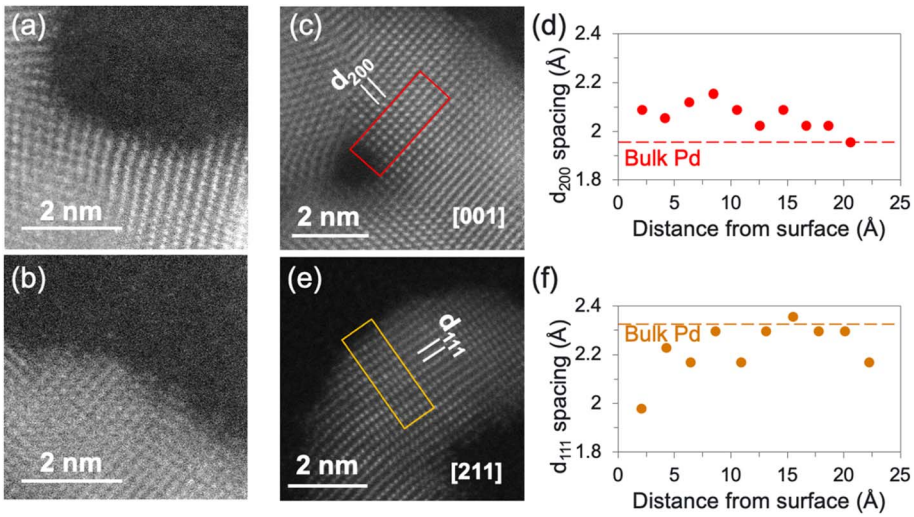

Fig. 4 The assemblies of Pd NPs (Pd gels) show concave and convex regions (a and b). The interactions between the merged NPs result in the distribution of local tensile (c and d) and compressive (e and f) strain fields near the sample surface.

discuss the results of the calculations performed using the Γ point. For completeness, the dependence of the calculated H incorporation energy and BZ and H adsorption energies on the k-mesh ($N \times N \times 1$, $N = 1, 2, 3$) and H_{sub} concentration is provided in Fig. S5.

First, we note that the calculated adsorption energy (E_{ads}) of an isolated H atom (H_{ads}) to the Pd(111) terrace is -0.7 eV, while the energy of H absorption (E_{abs}) into the subsurface Pd is -0.4 eV. Both E_{ads} and E_{abs} are calculated relative to 1/2 of a gas-phase H_2 molecule. While the energy gain due to H incorporation decreases with increasing H_{sub} concentration, H incorporation is thermodynamically favorable relative to the gas-phase H_2 up to an ML (see Fig. S5a); H_{sub} is further stabilized by the tensile strain (Fig. S6d). For comparison, the calculated E_{ads} of an isolated BZ molecule on Pd(111) terrace is -1.8 eV. Since the E_{ads} for BZ is approximately 2.4 times larger than that for H, BZ molecules are expected to displace H_{ads} from the Pd(111) surface. We and others indeed observe this displacement electrochemically, as discussed more in assessing the role of surface morphology in Section 3.3. The adsorbed BZ also affects the subsurface H (H_{sub}): while the H_{sub} species are not directly displaced by the BZ, the BZ modification of the surface structure and charge density distribution lowers the energy required to desorb H_{sub}. For example, in the case of a complete H_{sub} monolayer under a Pd(111) terrace without and with adsorbed BZ, extracting one H_{sub} as 1/2 H_2 requires 0.12 eV and less than 0.02 eV, respectively. As such, we anticipate H_{sub} to exit the lattice when BZ is adsorbed, possibly contributing to hydrogenation thermally, as discussed more in the context of our experimental measurements below.

In turn, H_{sub} has a destabilizing effect on the adsorbed BZ. To quantify this effect, we calculated E_{ads} of BZ on the Pd(111) surface in the presence of interstitial H in both ordered (2×2 and 3×3 planar arrangements within the supercell) and random distributions; in all cases, H_{sub} was located between the two outermost Pd planes. These calculations suggest that E_{ads} of BZ changes linearly with the H_{sub} content (Fig. 1b) from -1.8 eV per BZ molecule in pure Pd to -0.4 eV in a hypothetical PdH_x phase, where every subsurface octahedral site is occupied by H^- species. For comparison, we also examined the effect of H_{sub} on the hydrogen adsorption energy (Fig. 1b). Two to four H_{ads} configurations were considered for each H_{sub} concentration. The most stable among them also show a linear trend of lower adsorption energy with H_{sub} (Fig. 1b). However, the rate of this change is noticeably lower than in the case of BZ. It follows that in the case of a high H_{sub} concentration, E_{ads} values for H and BZ species are comparable, which would lead to competitive adsorption and affect the kinetics of their interactions.

Furthermore, since H absorption in Pd is accompanied by its volumetric expansion, the accumulation of H_{abs} species is expected to induce lateral strain. We mimic the applied strain by scaling the lateral supercell parameters by a factor of up to 1.02, corresponding to 2% linear expansion, consistent with experimentally observed localized strain resulting from hydride formation.[36] The calculated BZ E_{ads} values (Fig. 1c) suggest that the tensile strain stabilizes the adsorbed BZ in the case of a higher concentration of subsurface H but has little effect at lower concentrations. Finally, our calculations show that while tensile strain stabilizes H_{sub} (Fig. S6), these hydrogen species can spontaneously displace to the surface under the combined effects of strain and adsorbed BZ (Fig. S16), further supporting a potentially active role of H_{abs} in hydrogenation reactions under the conditions studied here.

3.2 The effect of Pd hydride on hydrogenation reactions

Having established the effect of the H_{sub} species on the BZ binding, we turn to the analysis of their impact on the rates of prototypical hydrogenation reactions, ECH and HER. To reveal

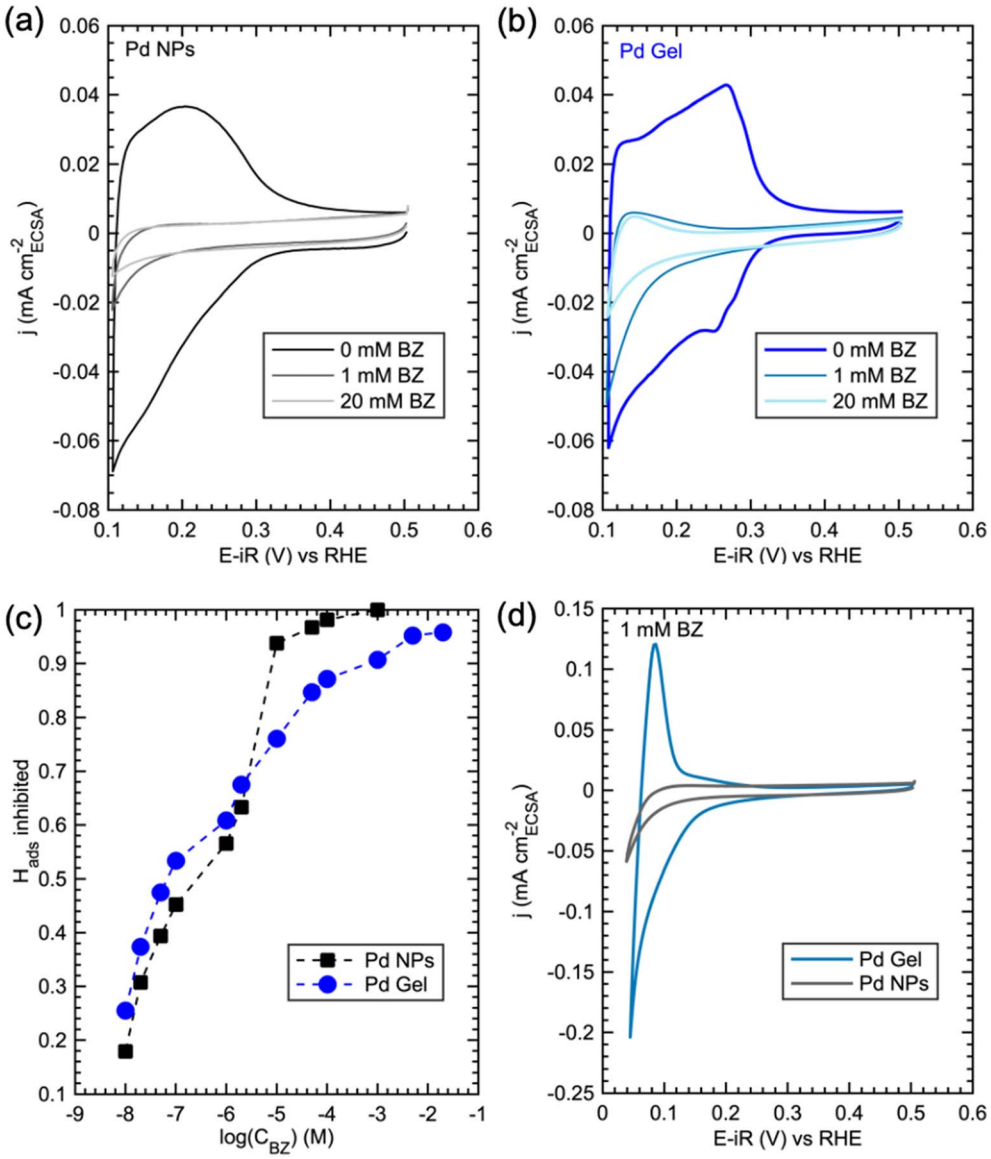

Fig. 5 Cyclic voltammetry at 20 mV s^{-1} in different concentrations of BZ for Pd NPs (a) and gel (b), where the amount of H_{ads} remaining can be considered *via* the integrated charge of its stripping above the baseline capacitance charge from the region. (c) Coverage of BZ (determined *via* H_{ads} inhibited) *vs.* its concentration (C_{BZ}) in solution. The dashed lines in (c) are to highlight the differences in the effect of C_{BZ} on H_{ads} in Pd NPs and Pd gel. (d) CV profiles demonstrate differences in the hydride formation in the presence of 1 mM BZ; measurements were performed at 20 mV s^{-1}.

the effect of the PdH_x phase, we prepared Pd NPs samples in the hydride (unstripped) and metallic (stripped) phases as described in Section 2. The reaction rates and the corresponding turnover frequencies (TOFs) at −0.1 V *vs.* RHE in 20 mM BZ solution are shown in Fig. 2 and S2, respectively, with additional data for a wider range of BZ concentrations shown in Fig. S3 and S4. The difference in the reaction rates is attributed to the absorbed H (H_{abs}), which may impact rates directly *via* thermal hydrogenation or indirectly by modifying the binding energy of surface adsorbates, as shown in Fig. 1b.[37–40] Despite the ability of H_{sub} to reduce BZ, the rate of BnOH production is higher for Pd metal (stripped) than for the hydride Pd (unstripped) NPs (Fig. 2a and S2a).

The apparent HER rate was calculated assuming that the total current (Table S1) is fully utilized to produce BnOH *via* ECH or H_2 *via* HER. The initial HER rate is approximately an order of magnitude higher for stripped Pd NPs (Fig. S2b), where only a negligible contribution from hydride formation can be expected given the high BZ concentration (C_{BZ} = 20 mM) and a strong binding of BZ to the Pd surfaces. These findings suggest that Pd metal also has a higher intrinsic rate towards HER than the Pd hydride, resulting in a lower ECH faradaic efficiency, FE, toward ECH (~70% *vs.* 90%, Table S2). These differences in rates and FEs illustrate the importance of catalyst history in considering the activity and selectivity of hydride-forming materials.

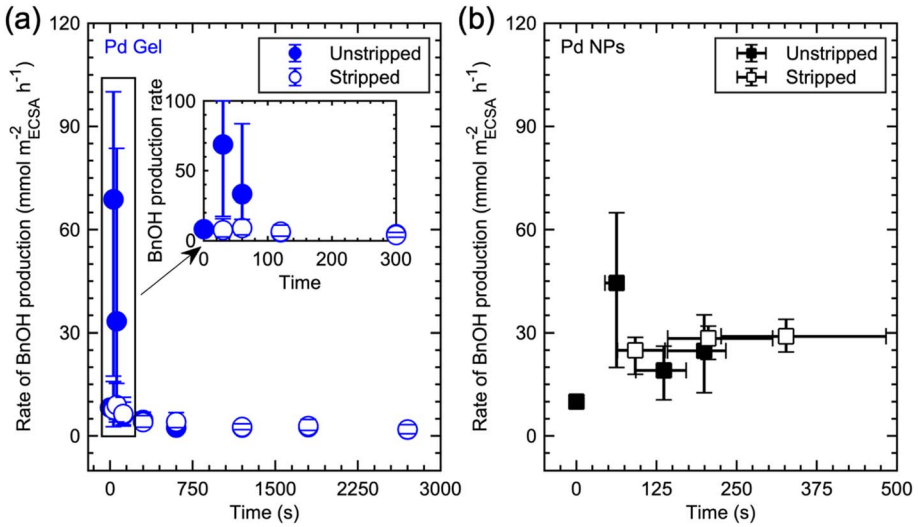

Fig. 6 Rate of BnOH production as a function of time in stripped and unstripped Pd in 1 mM BZ solution at −0.1 V *vs.* RHE: (a) Pd gel, (b) Pd NPs. BnOH production rate for the unstripped case at $t = 0$ (initial point taken after mixing 1 mM BZ for 5 min) is attributed to the activity of hydride. Error bars denote the maximum deviation from the average across three measurements.

3.3 The effect of Pd and PdH_x surface corrugation and morphology on competitive adsorption

Surfaces of nano-scale materials have a significant fraction of low-coordinated sites, where deviations from the flat terrace structure can modulate the binding of the reactants and affect kinetic rates. Here, we examine the effect of such surface corrugation by analyzing the combined effect of the H_{abs} and surface topography on BZ adsorption. Since the (111) termination is the prevalent surface facet in face-centered cubic crystals, and Σ3 (111) is the prevalent grain boundary, we represented corrugated surfaces using a periodic slab model containing (111) terraces and convex and concave regions formed by the intersections of Σ3 (111) GBs with surfaces (see Fig. S6). Similarly to the case of the flat terraces in Section 3.1, we find that H incorporation into the subsurface layer (H_{abs} formation) is favorable compared to gas-phase H_2 and stabilized by the presence of tensile strain in the [111] direction (Fig. S6 and 3).

To consider how the surface corrugation may influence BZ adsorption, we calculate BZ E_{ads} and characterize the charge density distributions for six configurations, defined by the proximity of the adsorbed BZ to the concave, flat, and convex regions (Fig. 3a). We find that BZ is most strongly bound at the (111) facets (configuration B in Fig. 3), while structural deviations from the (111) terraces arising from GBs have a destabilizing effect. For example, even in the case of configuration B, the confinement of the (111) facet provided by the concave and convex sites is sufficient to weaken the BZ adsorption energy from −1.8 eV, in the case of the infinite Pd(111) terrace, to −1.4 eV (Fig. 3b). Furthermore, in the vicinity of the convex features (configuration C), the C═O group does not directly interact with the Pd substrate, thus lowering the BZ adsorption energy even if the molecule remains essentially flat. In contrast, in the vicinity of concave features (configurations E and F), the BZ molecule undergoes deformation relative to its planar configuration in the gas phase, and the corresponding BZ E_{ads} can be as low as −0.8 eV and −0.2 eV for the metallic Pd and hydride Pd phases, respectively (Fig. 3b).

Subsurface H species weaken BZ binding to the surface by an additional ∼0.1–0.5 eV relative to configuration B. We attribute this effect to electron transfer from the host Pd to hydrogen atoms, forming $H^{\delta-}$ ($\delta = 0.06$). According to the Bader population analysis, 80% of this charge is transferred from the surface Pd atoms, which lowers their polarizability and, therefore, weakens the interactions with the BZ benzene ring. This effect is particularly pronounced in the case of the concave sites (configuration F), where strain variation may result in detachment of absorbed BZ from the surface, as suggested by the nearly identical BZ adsorption energies in configurations A and F at 0% strain. We also note that BZ E_{ads} at the concave site shows a strong strain dependence: tensile strain reduces the curvature of concave regions, leading to a stronger BZ-surface binding (Fig. 3b).

To obtain further insight into the factors that determine BZ E_{ads} magnitude, we deconvolute it into the contributions due to BZ deformation, *i.e.*, the energy penalty associated with the deviation of the BZ structure and charge distribution from those of the gas-phase BZ, and those due to attachment of the deformed BZ molecule to the corresponding surface site (Fig. S7). Plotting the BZ E_{ads} *vs.* the deformation energy reveals a V-shaped trend with the minimum corresponding to BZ at the (111) faces (Fig. 3c). Thus, deformation energies associated with adjusting the BZ structure and charge distribution to a surface site are most effectively offset by the energy of BZ attachment to this site in the case of the (111) terraces, and any topographic deviations from the flat terraces would result in weaker BZ E_{ads}. Therefore, we conclude that for NP assemblies with convex and concave regions in the vicinity of GBs between the NPs, weakened BZ interactions would limit the blocking of H_{ads} and enable the persistence of the PdH_x phase to higher C_{BZ}.

Applying the van der Waals (vdW) correction yields similar results. In particular, the BZ adsorption energies calculated with and without the vdW correction (Fig. S8) show the same trends for both pure Pd and PdH_x, except for configuration F. In the latter case, BZ adsorbed on the pure Pd conforms to the local curvature with and without vdW correction. However, accounting for the effects of polarization *via* the vdW correction suggests that, as the subsurface H weakens the BZ-surface interaction, it no longer compensates for the BZ deformation energy, resulting in a flat BZ configuration (Fig. S8d). These results further support the conclusion that concave sites on the Pd and PdH_x can remain exposed for H in-diffusion even at a high C_{BZ}.

To test these predictions, we compare the kinetics of electrocatalytic reduction of BZ for two types of samples: Pd nanoparticles (Pd NPs), which exhibit convex sites and terraces, and Pd gels formed by NPs assembled into quasi-one-dimensional (1D) structures that exhibit both convex and concave sites and inhomogeneous strain distribution (Fig. S9). High-resolution STEM images of Pd gels (Fig. 4) suggest that multiple NPs join together to form an open structure with a high density of GBs (see SI and Fig. S10) and convex and concave regions, leading to localized strain (Fig. 4d and f). Additional examples of the Pd gel structure at several magnifications and Pd gel XRD patterns are provided in Fig. S11 and S12, respectively.

To understand how the morphology of these systems influences the adsorption and intercalation of H and the subsequent formation of PdH_x, we consider the ability of BZ to block adsorbed H (H_{ads}) formed in aqueous electrochemical environments. H_{ads} amounts were quantified *via* the transfer of an electron (negative current) in the region of 0.35–0.1 V *vs.* RHE, and H removal was quantified by the positive current when sweeping from 0.1 to 0.35 V *vs.* RHE (Fig. 5a, b and S4). Increasing C_{BZ} in the solution led to higher BZ adsorption on the surface, blocking H_{ads}, in line with our calculations showing that BZ E_{ads} is greater than that of H. The extent of H_{ads} blocking was quantified *via* the difference in H_{ads} stripping charge,[19] where full H_{ads} inhibition reflects a maximum coverage of the surface by BZ (Fig. 5c and S4).

Both Pd NPs and Pd gels bind BZ strongly, consistent with the calculated BZ E_{ads} on the pure Pd(111) terrace discussed above (see also SI and Table S2 for an experimental assessment of E_{ads}). BZ adsorption to Pd gels weakens at $C_{BZ} > 10$ μM, as evidenced by the greater persistence of H_{ads} with increasing C_{BZ}. However, signatures of H_{ads} are still observed even at $C_{BZ} =$ 20 mM. In contrast, virtually no H_{ads} remain on Pd NPs for C_{BZ} of 100 μM and higher. This is consistent with the results of our *ab initio* calculations (Fig. 3), illustrating how strained and twinned regions, typical in Pd gels (Fig. 4), weaken BZ adsorption. The observed persistence of H_{ads} in Pd gels leads to the formation of the PdH_x phase, manifested by H_{ads} formation even at high (1 mM BZ) concentrations and observed *via* H stripping at ~0.08 V *vs.* RHE in the anodic sweep (Fig. 5d). Since a larger H_{ads} stripping charge for a given surface coverage of H_{ads} suggests a more facile hydrogen in-diffusion in Pd gel, we propose that a high density of GBs in Pd gels is responsible for this diffusion (Fig. S13). These observations suggest that the two types of Pd electrocatalysts likely demonstrate different behavior in BZ ECH reactions, particularly in the high C_{BZ} limit (C_{BZ} ~1 mM), where PdH_x might persist for the Pd gels (Fig. S14), but not NPs.

Finally, we note that the H_{ads} inhibition dependence on C_{BZ} for the Pd NP and Pd gel catalysts follows the same trend as C_{BZ} increases to $\log(C_{BZ}) = -5.5$ (Fig. 5c), indicating that similar surface regions (terraces and convex regions) are being affected by BZ in both samples. At higher C_{BZ}, the H_{ads} are completely displaced from the Pd NP surfaces, while they persist on the Pd gels until C_{BZ} is increased by an additional factor of ~10^3. We attribute these persistent H_{ads} to the concave regions in the gel structures that are unlikely to form in the NP samples but are present in abundance in Pd gels (see Fig. 4).

3.4 Using catalyst morphology to probe ECH performance depending on the subsurface H content

We concluded in Section 3.3 that Pd gel accommodates H_{abs} that persist even above 1 mM BZ (Fig. S13) and attributed the origin of such H_{abs} to concave sites associated with GBs, where BZ adsorption is weak due to the surface corrugation. We next consider the role of persistent subsurface H (H_{abs}) in the catalytic process.

The large initial rates of BnOH production on the unstripped PdH_x gels (Fig. 6) are likely due in part to a TCH contribution from subsurface H, given that the currents passed for stripped and unstripped are similar (Fig. S15). This proposition is supported by our *ab initio* calculations that show subsurface H (H_{abs}) can spontaneously transfer to the surface (H_{ads}) under 2% tensile strain (Fig. S16), and the experimental observation of rates converging for stripped and unstripped at times >100 s when H_{abs} content is likely similar. In contrast, the BnOH production rates of stripped and unstripped Pd NPs samples are largely similar (Fig. 6 and S17), indicating that the contribution of subsurface H to the TCH reaction is minimal. The distinction between the behaviors of unstripped NPs and gel samples suggests that the terraces and convex sites of NPs may favor subsurface H leaving the lattice as H_2, whereas the concave (and strained) sites of the Pd gel favor leaving the lattice *via* BZ hydrogenation.

Comparing the behavior of Pd gels and NPs in 1 mM BZ at longer times (>100 s), where TCH is negligible, showed a ~3*x* smaller BZ reduction rate for Pd gels (with some persistent H_{abs} based on adsorption measurements shown in Fig. 6) regardless of time or current passed (TOF *vs.* time, Fig S17 and 18). Together, these findings indicate that Pd hydride is not inherently more active than Pd metal for BZ ECH, but that subsurface H from preconditioning may contribute to thermal BZ reduction in conditions where its persistence in the lattice is unfavored (Fig. 6, S17 and Table S3). We note, however, that strain resultant from the formation of the hydride phase and inherent to the Pd gel morphology may also contribute to these observations. In particular, tensile strain leads to a slight upshift of the Pd d-band for both metal[41] and hydride phases (Fig. S19), and both hydride formation and strain result in the broadening

of the states nearest the Fermi level.[42–44] Hence, the strain inherent to the twin-boundary rich network may destabilize BZ relative to a more optimal binding on Pd NP surfaces.

To summarize, our experiments and simulation suggest the following mechanistic insight. BZ displaces adsorbed H in both stripped and non-stripped Pd NPs and gel samples. However, weaker BZ adsorption at concave regions in gels increases H_{ads} retention and allows for H transfer into the subsurface region, which in turn, further weakens the BZ binding to the surface. The higher concentration of pre-existing H_{abs} in gels is responsible for the initial higher activity observed in non-stripped gels, while the long-term effect of H_{abs} is negligible in all cases.

Together, these findings indicate that synthesis approaches should target control of the geometrical characteristics, density, and spatial distribution of the concave and convex regions in nanostructured catalysis as well as residual strain associated with these regions. Based on this work, we propose that the strength of interactions of organic molecules with metal surfaces can be controlled not only by their topography but also by the amount of subsurface hydrogen that can be retained at the surface and accumulated in the subsurface near concave regions and by the external strain that stabilizes these hydrogen species.

4 Conclusion

We examined the effect of surface corrugation, subsurface hydride phases, and strain in Pd nanoscale catalysts on the kinetics of characteristic hydrogenation reactions exemplified by BZ electroreduction. Isolated Pd nanoparticles that exhibit terraces and convex sites were used as a reference catalyst, while Pd-gel, in the form of interconnected quasi-1D chains containing a high density of grain boundaries, convex and concave sites, and strain, was used to provide insight into the role of structural inhomogeneities in the catalytic conversion. Our computational modeling predicts that concave surface sites are less susceptible to blocking by aromatic compounds, such as BZ, which allows hydrogen to be more readily incorporated into the Pd lattice and form the subsurface PdH_x phase. This is consistent with our experimental measurement of persistent hydride formation in Pd gels at higher BZ concentrations than for Pd NPs, which do not have these convex sites. However, as the hydride phase is not stable for NPs over these concentrations—our calculations confirm it prefers to leave the lattice—we find it contributes to the rate of BnOH formation at short timescales, providing a new lens through which to consider previous reports starting with the hydride phase. In fact, we find the metallic starting phase has higher HER and ECH rates, but lower FE towards BZ ECH.

Calculations show tensile strain enhances the PdH_x stability, which, in turn, weakens the BZ interaction with Pd surfaces. The effect of these processes on the hydrogenation reaction was analyzed by comparing the kinetics of BZ reduction on the NP and gel samples. The Pd gel has a lower rate for BZ ECH than Pd NPs, consistent with weakened BZ adsorption on the gel resultant from tensile strain associated with grain boundaries and residual hydride phase. Although the ECH rate for this model reaction is lower for gels, this work demonstrates how structurally complex samples in the form of gels provide degrees of freedom for controlling the behavior of metal catalysts that are not available in NP catalysts, which paves the way for new approaches in the design of catalytic materials.

Author contributions

K. A. S., S. K. M. P., and P. V. S. have conceived the study; S. K. M. P. and K. A. S. performed the electrochemical measurements and analysis; S. N., K. A. U. M., and L. L. prepared the Pd samples; D. L. and H. P. performed microscopic characterization and analysis; H. Z. performed XRD characterization and analysis; N. C., Q. P., and P. V. S. performed *ab initio* simulations. The manuscript was written by S. K. M. P., K. A. S., and P. V. S. with contributions from all co-authors. All co-authors have commented on and approved the final version.

Conflicts of interest

There are no conflicts to declare.

Data availability

The data supporting this article have been included as part of the SI. See DOI: **https://doi.org/10.1039/d5ta05129k**.

Acknowledgements

This work was supported by the U.S. Department of Energy (DOE) Office of Science (SC), Basic Energy Sciences, Materials Sciences and Engineering Division, Synthesis and Processing Science Program, FWP 78705. This research used resources of the National Energy Research Scientific Computing Center, a DOE Office of Science User Facility supported by the Office of Science of the U.S. DOE under Contract No. DE-AC02-05CH11231 using NERSC award BES-ERCAP0033807. Pacific Northwest National Laboratory is a multiprogram national laboratory operated for DOE by Battelle under contract DE-AC05-76RL01830. This research used resources of the Advanced Photon Source, a U.S. DOE SC User Facility, operated for the DOE SC by Argonne National Laboratory under Contract No. DE-AC02-06CH11357. We thank R. M. Boiteau for assistance with RP-HPLC measurements.

References

1 R. S. Sherbo, A. Kurimoto, C. M. Brown and C. P. Berlinguette, Efficient Electrocatalytic Hydrogenation with a Palladium Membrane Reactor, *J. Am. Chem. Soc.*, 2019, **141**(19), 7815–7821.
2 A. Ngoipala, R. Lipin, R. L. Arevalo and M. Vandichel, Computational unravelling of cathodic hydride formation on palladium surfaces, *Int. J. Hydrogen Energy*, 2024, **53**, 829–839.

3 H. Wang, Y. Qin, Y. Wu, Y. Qiu, L. Ling, Q. Fang, C. Wang, L. Hu, W. Gu and C. Zhu, Pd hydride metallene aerogels with lattice hydrogen participation for efficient hydrogen evolution reaction, *Nat. Commun.*, 2024, **15**(1), 10289.
4 M. D. Stankovic, B. Ge, J. F. Sperryn and C. P. Berlinguette, Electrochemical Control of Heterolytic and Homolytic Hydrogenation Pathways at a Palladium Surface, *J. Am. Chem. Soc.*, 2025, **147**(13), 10974–10980.
5 Y. Luo, Q. Wang, J. Li, F. Xu, L. Sun, Y. Zou, H. Chu, B. Li and K. Zhang, Enhanced hydrogen storage/sensing of metal hydrides by nanomodification, *Mater. Today Nano*, 2020, **9**, 100071.
6 J. Zhang, Y. Zhu, H. Lin, Y. Liu, Y. Zhang, S. Li, Z. Ma and L. Li, Metal Hydride Nanoparticles with Ultrahigh Structural Stability and Hydrogen Storage Activity Derived from Microencapsulated Nanoconfinement, *Adv. Mater.*, 2017, **29**(24), 1700760.
7 A. Schneemann, J. L. White, S. Kang, S. Jeong, L. F. Wan, E. S. Cho, T. W. Heo, D. Prendergast, J. J. Urban, B. C. Wood, M. D. Allendorf and V. Stavila, Nanostructured Metal Hydrides for Hydrogen Storage, *Chem. Rev.*, 2018, **118**(22), 10775–10839.
8 R. Smoluchowski, Anisotropy of the Electronic Work Function of Metals, *Phys. Rev.*, 1941, **60**(9), 661–674.
9 R. Duś, R. Nowakowski and E. Nowicka, Chemical and structural components of work function changes in the process of palladium hydride formation within thin Pd film, *J. Alloys Compd.*, 2005, **404–406**, 284–287.
10 J. A. Mwanda and A. Cuesta, Reduction of Pd2+ pre-adsorbed on cyanide-modified Pt(111) electrodes: Adlayer metallization *vs.* metal-on-metal deposition, *Electrochim. Acta*, 2018, **292**, 419–424.
11 S. K. M. Padavala and K. A. Stoerzinger, Role of Hydride Formation in Electrocatalysis for Sustainable Chemical Transformations, *ACS Catal.*, 2023, **13**(7), 4544–4551.
12 J. H. Lee, S. Kattel, Z. Jiang, Z. Xie, S. Yao, B. M. Tackett, W. Xu, N. S. Marinkovic and J. G. Chen, Tuning the activity and selectivity of electroreduction of CO2 to synthesis gas using bimetallic catalysts, *Nat. Commun.*, 2019, **10**(1), 3724.
13 L. C. Meyer, U. Sanyal, K. A. Stoerzinger, K. Koh, J. L. Fulton, D. M. Camaioni, O. Y. Gutiérrez and J. A. Lercher, Influence of the Molecular Structure on the Electrocatalytic Hydrogenation of Carbonyl Groups and H2 Evolution on Pd, *ACS Catal.*, 2022, **12**(19), 11910–11917.
14 S. A. Akhade, N. Singh, O. Y. Gutiérrez, J. Lopez-Ruiz, H. Wang, J. D. Holladay, Y. Liu, A. Karkamkar, R. S. Weber, A. B. Padmaperuma, M.-S. Lee, G. A. Whyatt, M. Elliott, J. E. Holladay, J. L. Male, J. A. Lercher, R. Rousseau and V.-A. Glezakou, Electrocatalytic Hydrogenation of Biomass-Derived Organics: A Review, *Chem. Rev.*, 2020, **120**(20), 11370–11419.
15 S. A. Akhade, M.-S. Lee, L. C. Meyer, S. F. Yuk, M.-T. Nguyen, U. Sanyal, J. D. Egbert, O. Y. Gutiérrez, V.-A. Glezakou and R. Rousseau, Impact of functional groups on the electrocatalytic hydrogenation of aromatic carbonyls to alcohols, *Catal. Today*, 2022, **397–399**, 63–68.
16 J. A. Lopez-Ruiz, E. Andrews, S. A. Akhade, M.-S. Lee, K. Koh, U. Sanyal, S. F. Yuk, A. J. Karkamkar, M. A. Derewinski, J. Holladay, V.-A. Glezakou, R. Rousseau, O. Y. Gutiérrez and J. D. Holladay, Understanding the Role of Metal and Molecular Structure on the Electrocatalytic Hydrogenation of Oxygenated Organic Compounds, *ACS Catal.*, 2019, **9**(11), 9964–9972.
17 J. A. Lopez-Ruiz, U. Sanyal, J. Egbert, O. Y. Gutiérrez and J. Holladay, Kinetic Investigation of the Sustainable Electrocatalytic Hydrogenation of Benzaldehyde on Pd/C: Effect of Electrolyte Composition and Half-Cell Potentials, *ACS Sustain. Chem. Eng.*, 2018, **6**(12), 16073–16085.
18 U. Sanyal, S. F. Yuk, K. Koh, M.-S. Lee, K. Stoerzinger, D. Zhang, L. C. Meyer, J. A. Lopez-Ruiz, A. Karkamkar, J. D. Holladay, D. M. Camaioni, M.-T. Nguyen, V.-A. Glezakou, R. Rousseau, O. Y. Gutiérrez and J. A. Lercher, Hydrogen Bonding Enhances the Electrochemical Hydrogenation of Benzaldehyde in the Aqueous Phase, *Angew. Chem., Int. Ed.*, 2021, **60**(1), 290–296.
19 N. Singh, U. Sanyal, G. Ruehl, K. A. Stoerzinger, O. Y. Gutiérrez, D. M. Camaioni, J. L. Fulton, J. A. Lercher and C. T. Campbell, Aqueous phase catalytic and electrocatalytic hydrogenation of phenol and benzaldehyde over platinum group metals, *J. Catal.*, 2020, **382**, 372–384.
20 Y. Song, U. Sanyal, D. Pangotra, J. D. Holladay, D. M. Camaioni, O. Y. Gutiérrez and J. A. Lercher, Hydrogenation of benzaldehyde *via* electrocatalysis and thermal catalysis on carbon-supported metals, *J. Catal.*, 2018, **359**, 68–75.
21 J. D. Benck, A. Jackson, D. Young, D. Rettenwander and Y.-M. Chiang, Producing High Concentrations of Hydrogen in Palladium *via* Electrochemical Insertion from Aqueous and Solid Electrolytes, *Chem. Mater.*, 2019, **31**(11), 4234–4245.
22 C. C. Hu and T. C. Wen, Effects of pH and Anion on Hydrogen Sorption/Desorption at/within Oxide-Derived Pd Electrodes, *J. Electrochem. Soc.*, 1995, **142**(5), 1376.
23 A. Zalineeva, S. Baranton, C. Coutanceau and G. Jerkiewicz, Octahedral palladium nanoparticles as excellent hosts for electrochemically adsorbed and absorbed hydrogen, *Sci. Adv.*, 2017, **3**(2), e1600542.
24 E. Andrews, J. A. Lopez-Ruiz, J. D. Egbert, K. Koh, U. Sanyal, M. Song, D. Li, A. J. Karkamkar, M. A. Derewinski, J. Holladay, O. Y. Gutiérrez and J. D. Holladay, Performance of Base and Noble Metals for Electrocatalytic Hydrogenation of Bio-Oil-Derived Oxygenated Compounds, *ACS Sustain. Chem. Eng.*, 2020, **8**(11), 4407–4418.
25 K. Koh, U. Sanyal, M.-S. Lee, G. Cheng, M. Song, V.-A. Glezakou, Y. Liu, D. Li, R. Rousseau, O. Y. Gutiérrez, A. Karkamkar, M. Derewinski and J. A. Lercher, Electrochemically Tunable Proton-Coupled Electron Transfer in Pd-Catalyzed Benzaldehyde Hydrogenation, *Angew. Chem., Int. Ed.*, 2020, **59**(4), 1501–1505.
26 X. Geng, S. Li, J. Heo, Y. Peng, W. Hu, Y. Liu, J. Huang, Y. Ren, D. Li, L. Zhang and L. Luo, Grain-Boundary-Rich Noble Metal Nanoparticle Assemblies: Synthesis,

Characterization, and Reactivity, *Adv. Funct. Mater.*, 2022, **32**(34), 2204169.
27 G. Kresse and J. Furthmüller, Efficient iterative schemes for *ab initio* total-energy calculations using a plane-wave basis set, *Phys. Rev. B: Condens. Matter Mater. Phys.*, 1996, **54**(16), 11169–11186.
28 G. Kresse and D. Joubert, From ultrasoft pseudopotentials to the projector augmented-wave method, *Phys. Rev. B: Condens. Matter Mater. Phys.*, 1999, **59**(3), 1758–1775.
29 J. P. Perdew, K. Burke and M. Ernzerhof, Generalized Gradient Approximation Made Simple, *Phys. Rev. Lett.*, 1996, **77**(18), 3865–3868.
30 P. E. Blöchl, Projector augmented-wave method, *Phys. Rev. B: Condens. Matter Mater. Phys.*, 1994, **50**(24), 17953–17979.
31 S. Grimme, J. Antony, S. Ehrlich and H. Krieg, A consistent and accurate *ab initio* parametrization of density functional dispersion correction (DFT-D) for the 94 elements H-Pu, *J. Chem. Phys.*, 2010, **132**(15), 154104.
32 W. Tang, E. Sanville and G. Henkelman, A grid-based Bader analysis algorithm without lattice bias, *J. Phys.: Condens. Matter*, 2009, **21**(8), 084204.
33 M. Yu and D. R. Trinkle, Accurate and efficient algorithm for Bader charge integration, *J. Chem. Phys.*, 2011, **134**(6), 064111.
34 S. Henning, J. Herranz and H. A. Gasteiger, Bulk-Palladium and Palladium-on-Gold Electrocatalysts for the Oxidation of Hydrogen in Alkaline Electrolyte, *J. Electrochem. Soc.*, 2014, **162**(1), F178–F189.
35 H. S. I. Tan, M. A. Manning, M.-K. Hahn, H. G. H. Tan and U. R. Kotagal, Determination of benzyl alcohol and its metabolite in plasma by reversed-phase high-performance liquid chromatography, *J. Chromatogr. B Biomed. Sci. Appl.*, 1991, **568**(1), 145–155.
36 K. Madhushani, H. Park, H. Zhou, D. Mal, Q. Pang, D. Li, P. Sushko and L. Luo, Σ3 (111) Grain Boundaries Accelerate Hydrogen Insertion into Palladium Nanostructures, *ChemRxiv*, 2025.
37 M. Johansson, E. Skúlason, G. Nielsen, S. Murphy, R. M. Nielsen and I. Chorkendorff, Hydrogen adsorption on palladium and palladium hydride at 1bar, *Surf. Sci.*, 2010, **604**(7), 718–729.
38 P. A. Sheth, M. Neurock and C. M. Smith, A First-Principles Analysis of Acetylene Hydrogenation over Pd(111), *J. Phys. Chem. B*, 2003, **107**(9), 2009–2017.
39 F. Studt, F. Abild-Pedersen, T. Bligaard, R. Z. Sørensen, C. H. Christensen and J. K. Nørskov, On the Role of Surface Modifications of Palladium Catalysts in the Selective Hydrogenation of Acetylene, *Angew. Chem., Int. Ed.*, 2008, **47**(48), 9299–9302.
40 M. Wilde, K. Fukutani, W. Ludwig, B. Brandt, J.-H. Fischer, S. Schauermann and H.-J. Freund, Influence of Carbon Deposition on the Hydrogen Distribution in Pd Nanoparticles and Their Reactivity in Olefin Hydrogenation, *Angew. Chem., Int. Ed.*, 2008, **47**(48), 9289–9293.
41 E. M. Dietze and H. Grönbeck, Structure-Dependent Strain Effects, *ChemPhysChem*, 2020, **21**(21), 2407–2410.
42 S. Mizusaki, N. Hiraoka, I. Yamamoto, M. Itou, Y. Sakurai and M. Yamaguchi, Electronic Structure of the Palladium Hydride Studied by Compton Scattering, *J. Phys. Soc. Jpn.*, 2003, **72**(5), 1145–1151.
43 J. Zbasnik and M. Mahnig, The electronic structure of beta-phase palladium hydride, *Z. Phys. B Condens. Matter*, 1976, **23**(1), 15–21.
44 P. A. Bennett and J. C. Fuggle, Electronic structure and surface kinetics of palladium hydride studied with x-ray photoelectron spectroscopy and electron-energy-loss spectroscopy, *Phys. Rev. B: Condens. Matter Mater. Phys.*, 1982, **26**(11), 6030–6039.